

A new hybrid finite element approach for three-dimensional elastic problems

C. CAO¹⁾, Q.-H. QIN¹⁾, A. YU²⁾

¹⁾ *Research School of Engineering
Australian National University
Canberra, ACT 0200, Australia
e-mail: qinghua.qin@anu.edu.au*

²⁾ *School of Materials Science and Engineering
The University of New South Wales
Sydney, NSW 2052, Australia*

A NEW FUNDAMENTAL SOLUTION based finite element method (HFS-FEM) is presented for analyzing three-dimensional (3D) elastic problems with body forces in this paper. It begins with deriving formulations of 3D HFS-FEM for elastic problems without body force and then the body force term is handled by means of the method of particular solution and radial basis function approximation. In our analysis, the homogeneous solution is obtained using the proposed HFS-FEM and the particular solution associated with the body force is approximated by radial basis functions. Several standard tests and numerical examples are considered to assess the capability and performance of the proposed method and elements. It is found that, comparing with conventional FEM (ABAQUS), the proposed method can achieve higher accuracy and efficiency when same element meshes are used. It is also found that the elements associated with this method are not very sensitive to mesh distortion and can be employed for problems involving nearly incompressible materials. This new method seems to be promising to deal with problems involving generalized body force, complex geometry, stress concentration and multi-materials.

Key words: fundamental solution, hybrid finite element method (FEM), 3D elasticity, body force, particular solution, radial basis function (RBF).

Copyright © 2012 by IPPT PAN

1. Introduction

DURING THE PAST THREE DECADES, Hybrid Trefftz finite element method (HT-FEM), as a significant alternative to conventional FEM, has become popular and been increasingly used to analyze various engineering problems [1–13]. In contrast to conventional FEM, HT-FEM is based on a hybrid method which includes the use of an independent auxiliary inter-element frame field defined on element boundary and an independent internal field chosen so as a prior satisfying the homogeneous governing differential equations by means of a suitable truncated

T-complete function set of homogeneous solutions [14]. Inter-element continuity is enforced by employing a modified variational principle, which is used to construct standard stiffness equation, and to establish the relationship between the frame field and the internal field of the element. The property of nonsingular element boundary integral appeared in HT-FEM enables us to construct arbitrarily shaped element conveniently; however, the terms of truncated T-complete functions should be carefully selected for achieving desired results and the T-complete functions for some physical problems are difficult to generate [15].

To remove the drawback of HT-FEM, a novel hybrid FE formulation based on the fundamental solution, named as HFS-FEM, was firstly developed for solving two dimensional heat conduction problem in single and multi-materials [16, 17]. It has demonstrated good performance in 2D elastic [18] and piezoelectric problems [19] by employing fundamental solutions to substitute for the T-complete functions in HT-FEM as a trial function. In this approach, the intra-element field is approximated by a linear combination of fundamental functions analytically satisfying the related governing equations, the independent frame field defined along the element boundary and the newly developed variational functional are employed to guarantee the inter-element continuity, generate the final stiffness equation, and establish the relationship between boundary frame field and internal field of the element under consideration.

In the HFS-FEM, the domain integrals in the hybrid functional can be directly converted into boundary integrals without any appreciable increase in computational effort and no singular integrals are involved by locating the source point outside the element of interest and not overlap with field point during the computation [18]. Moreover, the features of two independent interpolation fields and element boundary integral in HFS-FEM make the algorithm have potential applications in the aspect of mesh reduction by constructing specially-purposed elements such as functionally graded element, hole element, crack element etc. [9, 20, 21]. The proposed HFS-FEM inherits all advantages of HT-FEM and removes the difficulty in constructing and selecting T-functions, so it has the capacity to be applied to more extensive applications than HT-FEM. In addition, it should be pointed out that the developed HFS-FEM approach is different from the BEM, although the same fundamental solution is employed. Using the reciprocal theorem, the BEM obtains the boundary integral equation, which usually encounters difficulty in dealing with singular or hyper-singular integrals in the BEM analysis, while the weakness can be removed using HFS-FEM. Additionally, HFS-FEM makes it possible for a more flexible element material definition which is important in dealing with multi-material problems, rather than the material definition being the same in the entire domain in BEM. However, to the authors' knowledge, there is no work reported in the literature on the application of this promising method to 3D elastic problems.

In this paper, a new solution procedure based on HFS-FEM approach is proposed to solve three-dimensional elastic problems with/without body forces. The detailed 3D formulations of HFS-FEM are firstly derived for elastic problems by ignoring body forces, then a procedure based on the method of particular solution and radial basis function approximation are presented to deal with the body force. As a consequence, the homogeneous solution is obtained by using the HFS-FEM and the particular solution associated with body force is approximated by using the strong form basis function interpolation. The solution procedure for three-dimensional elastostatic problems is then programmed by means of MATLAB. Several standard tests and numerical examples are investigated and their results are compared with the existing closed-form solutions or ABAQUS results. The results show that the proposed method has higher accuracy and efficiency than ABAQUS when using same element meshes. It is also found that this method is not sensitive to mesh distortion and has capability to deal with nearly incompressible materials.

2. Formulations of the HFS-FEM for 3D elasticity without the body force

2.1. Governing equations and boundary conditions

In this subsection, basic equations commonly used in literatures are briefly reviewed to provide notations for the subsequent sections. Let (X_1, X_2, X_3) denote the coordinates in Cartesian coordinate system and consider a finite isotropic body occupying the domain Ω , as shown in Fig. 1. The equilibrium equation for this finite body in the absence of body force can be expressed as

$$(2.1) \quad \sigma_{ij,j} = 0, \quad i, j = 1, 2, 3.$$

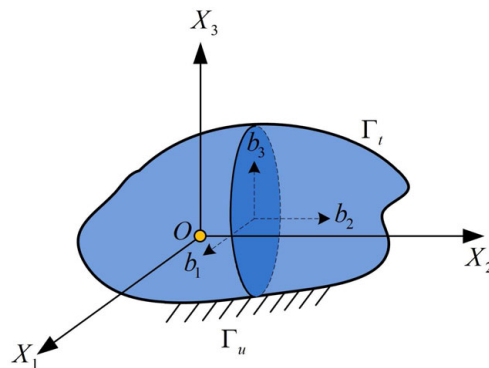


FIG. 1. Geometrical definitions and boundary conditions for a general 3D solid.

The constitutive equations for linear elasticity and the kinematical relation are given as

$$(2.2) \quad \sigma_{ij} = \frac{2Gv}{1-2v} \delta_{ij} e_{kk} + 2G e_{ij},$$

$$(2.3) \quad e_{ij} = \frac{1}{2}(u_{i,j} + u_{j,i}),$$

where σ_{ij} is the stress tensor, e_{ij} the strain tensor, u_i the displacement vector, δ_{ij} the Kronecker delta, G the shear modulus, and v Poisson's ratio. Substituting Eq. (2.2) and (2.3) into Eq. (2.1), the equilibrium equations may be rewritten in terms of displacements as

$$(2.4) \quad G u_{i,jj} + \frac{G}{1-2v} u_{j,ji} = 0.$$

For a well-posed boundary value problem, following boundary conditions, either displacement or traction boundary condition, are prescribed as

$$(2.5) \quad u_i = \bar{u}_i \quad \text{on } \Gamma_u,$$

$$(2.6) \quad t_i = \bar{t}_i \quad \text{on } \Gamma_t,$$

where $\Gamma_u \cup \Gamma_t = \Gamma$ is the boundary of the solution domain Ω , \bar{u}_i and \bar{t}_i are the prescribed boundary values.

2.2. Assumed fields

To solve the problem governed by Eqs. (2.4)–(2.6) using HFS-FEM approach, the solution domain Ω is divided into a series of elements as done in conventional FEM. For each element, two independent fields, i.e. intra-element field and frame field, are assumed in a manner as that presented in [16, 18]. The main idea of the HFS-FEM is to establish a FE formulation whereby intra-element continuity is enforced on a nonconforming internal displacement field chosen as the fundamental solution of the problem under consideration [18]. In this approach, the intra-element displacement field is approximated in terms of a linear combination of fundamental solutions of the problem as

$$(2.7) \quad \mathbf{u}(\mathbf{x}) = \begin{Bmatrix} u_1(\mathbf{x}) \\ u_2(\mathbf{x}) \\ u_3(\mathbf{x}) \end{Bmatrix} = \mathbf{N}_e \quad \mathbf{c}_e \quad (\mathbf{x} \in \Omega_e, \mathbf{y}_{sj} \notin \Omega_e),$$

where the matrix \mathbf{N}_e and unknown vector \mathbf{c}_e can be further written as

$$(2.8) \quad \mathbf{N}_e = \begin{bmatrix} u_{11}^*(\mathbf{x}, \mathbf{y}_{s1}) & u_{12}^*(\mathbf{x}, \mathbf{y}_{s1}) & u_{13}^*(\mathbf{x}, \mathbf{y}_{s1}) & \cdots & u_{11}^*(\mathbf{x}, \mathbf{y}_{sn_s}) & u_{12}^*(\mathbf{x}, \mathbf{y}_{sn_s}) & u_{13}^*(\mathbf{x}, \mathbf{y}_{sn_s}) \\ u_{21}^*(\mathbf{x}, \mathbf{y}_{s1}) & u_{22}^*(\mathbf{x}, \mathbf{y}_{s1}) & u_{23}^*(\mathbf{x}, \mathbf{y}_{s1}) & \cdots & u_{21}^*(\mathbf{x}, \mathbf{y}_{sn_s}) & u_{22}^*(\mathbf{x}, \mathbf{y}_{sn_s}) & u_{23}^*(\mathbf{x}, \mathbf{y}_{sn_s}) \\ u_{31}^*(\mathbf{x}, \mathbf{y}_{s1}) & u_{32}^*(\mathbf{x}, \mathbf{y}_{s1}) & u_{33}^*(\mathbf{x}, \mathbf{y}_{s1}) & \cdots & u_{31}^*(\mathbf{x}, \mathbf{y}_{sn_s}) & u_{32}^*(\mathbf{x}, \mathbf{y}_{sn_s}) & u_{33}^*(\mathbf{x}, \mathbf{y}_{sn_s}) \end{bmatrix}$$

$$(2.9) \quad \mathbf{c}_e = [c_{11} \ c_{21} \ c_{31} \ \cdots \ c_{1n} \ c_{2n} \ c_{3n}]^T,$$

in which \mathbf{x} and \mathbf{y}_{sj} are respectively the field point and source point in the local coordinate system (X_1, X_2) . The components $u_{ij}^*(\mathbf{x}, \mathbf{y}_{sj})$ is the fundamental solution, i.e. induced displacement component in i -direction at the field point \mathbf{x} due to a unit point load applied in j -direction at the source point \mathbf{y}_{sj} placed outside the element, which are given by [22]

$$(2.10) \quad u_{ij}^*(\mathbf{x}, \mathbf{y}_{sj}) = \frac{1}{16\pi(1-\nu)Gr} \{(3-4\nu)\delta_{ij} + r_{,i}r_{,j}\},$$

where $r_i = x_i - x_{is}$, $r = \sqrt{r_1^2 + r_2^2 + r_3^2}$, n_s is the number of source points.

In our analysis, the number of source points is taken to be the same as the number of element nodes, which is free of spurious energy modes and can keep the stiffness equations in full rank, as indicated in [14]. The source point \mathbf{y}_{sj} ($j = 1, 2, \dots, n_s$) can be generated by means of the following method [18]

$$(2.11) \quad \mathbf{y}_s = \mathbf{x}_0 + \gamma(\mathbf{x}_0 - \mathbf{x}_c),$$

where γ is a dimensionless coefficient, \mathbf{x}_0 is the point on the element boundary (the nodal point in this work) and \mathbf{x}_c the geometrical centroid of the element (see Fig. 2). Determination of γ was discussed in [17, 18] and $\gamma = 8$ is used in the following analysis.

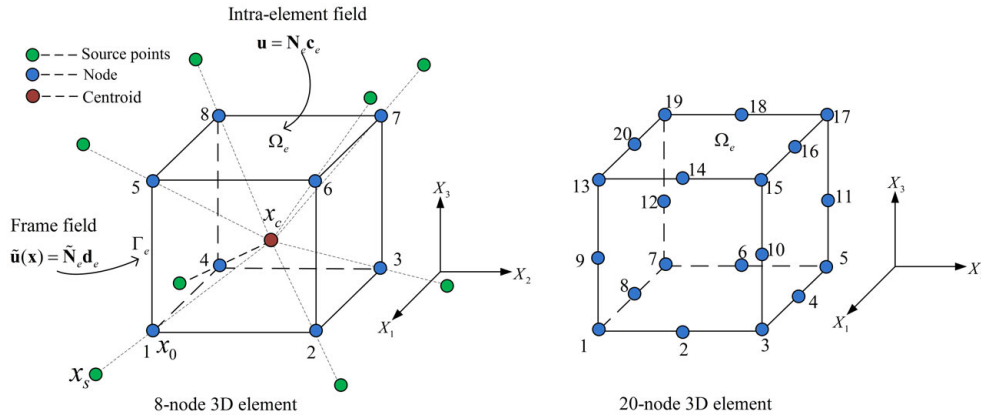


FIG. 2. Intra-element field and frame field of a hexahedron HFS-FEM element for 3D elastic problem (the source points and centroid of 20-node element are omitted in the figure for clarity and clear view, which is similar to that of the 8-node element).

According to Eqs. (2.2) and (2.3), the corresponding stress fields can be expressed as

$$(2.12) \quad \sigma(\mathbf{x}) = [\sigma_{11} \ \sigma_{22} \ \sigma_{33} \ \sigma_{23} \ \sigma_{31} \ \sigma_{12}]^T = \mathbf{T}_e \mathbf{c}_e,$$

where

$$(2.13) \quad \mathbf{T}_e = \begin{bmatrix} \sigma_{111}^*(\mathbf{x}, \mathbf{y}_1) & \sigma_{211}^*(\mathbf{x}, \mathbf{y}_1) & \sigma_{311}^*(\mathbf{x}, \mathbf{y}_1) & \cdots & \sigma_{111}^*(\mathbf{x}, \mathbf{y}_{n_s}) & \sigma_{211}^*(\mathbf{x}, \mathbf{y}_{n_s}) & \sigma_{311}^*(\mathbf{x}, \mathbf{y}_{n_s}) \\ \sigma_{122}^*(\mathbf{x}, \mathbf{y}_1) & \sigma_{222}^*(\mathbf{x}, \mathbf{y}_1) & \sigma_{322}^*(\mathbf{x}, \mathbf{y}_1) & \cdots & \sigma_{122}^*(\mathbf{x}, \mathbf{y}_{n_s}) & \sigma_{222}^*(\mathbf{x}, \mathbf{y}_{n_s}) & \sigma_{322}^*(\mathbf{x}, \mathbf{y}_{n_s}) \\ \sigma_{133}^*(\mathbf{x}, \mathbf{y}_1) & \sigma_{233}^*(\mathbf{x}, \mathbf{y}_1) & \sigma_{333}^*(\mathbf{x}, \mathbf{y}_1) & \cdots & \sigma_{133}^*(\mathbf{x}, \mathbf{y}_{n_s}) & \sigma_{233}^*(\mathbf{x}, \mathbf{y}_{n_s}) & \sigma_{333}^*(\mathbf{x}, \mathbf{y}_{n_s}) \\ \sigma_{123}^*(\mathbf{x}, \mathbf{y}_1) & \sigma_{223}^*(\mathbf{x}, \mathbf{y}_1) & \sigma_{323}^*(\mathbf{x}, \mathbf{y}_1) & \cdots & \sigma_{123}^*(\mathbf{x}, \mathbf{y}_{n_s}) & \sigma_{223}^*(\mathbf{x}, \mathbf{y}_{n_s}) & \sigma_{323}^*(\mathbf{x}, \mathbf{y}_{n_s}) \\ \sigma_{131}^*(\mathbf{x}, \mathbf{y}_1) & \sigma_{231}^*(\mathbf{x}, \mathbf{y}_1) & \sigma_{331}^*(\mathbf{x}, \mathbf{y}_1) & \cdots & \sigma_{131}^*(\mathbf{x}, \mathbf{y}_{n_s}) & \sigma_{231}^*(\mathbf{x}, \mathbf{y}_{n_s}) & \sigma_{331}^*(\mathbf{x}, \mathbf{y}_{n_s}) \\ \sigma_{112}^*(\mathbf{x}, \mathbf{y}_1) & \sigma_{212}^*(\mathbf{x}, \mathbf{y}_1) & \sigma_{312}^*(\mathbf{x}, \mathbf{y}_1) & \cdots & \sigma_{112}^*(\mathbf{x}, \mathbf{y}_{n_s}) & \sigma_{212}^*(\mathbf{x}, \mathbf{y}_{n_s}) & \sigma_{312}^*(\mathbf{x}, \mathbf{y}_{n_s}) \end{bmatrix}.$$

The components $\sigma_{ijk}^*(\mathbf{x}, \mathbf{y})$ is given by

$$(2.14) \quad \sigma_{ijk}^*(\mathbf{x}, \mathbf{y}) = \frac{-1}{8\pi(1-\nu)r^2} \{(1-2\nu)(r_{,k}\delta_{ij} + r_{,j}\delta_{ki} - r_{,i}\delta_{jk}) + 3r_{,i}r_{,j}r_{,k}\}.$$

As a consequence, the traction can be written in the form

$$(2.15) \quad \begin{Bmatrix} t_1 \\ t_2 \\ t_3 \end{Bmatrix} = \mathbf{n}\boldsymbol{\sigma} = \mathbf{Q}_e\mathbf{c}_e,$$

in which

$$(2.16) \quad \mathbf{Q}_e = \mathbf{n}\mathbf{T}_e, \quad \mathbf{n} = \begin{bmatrix} n_1 & 0 & 0 & 0 & n_3 & n_2 \\ 0 & n_2 & 0 & n_3 & 0 & n_1 \\ 0 & 0 & n_3 & n_2 & n_1 & 0 \end{bmatrix}.$$

The unknown \mathbf{c}_e in Eqs. (2.7) and (2.12) may be calculated using a hybrid technique [17], in which the elements are linked through an auxiliary conforming displacement frame which has the same form as in conventional FEM (see Fig. 2). This means that in the HFS-FEM, a conforming displacement field should be independently defined on the element boundary to enforce the field continuity between elements and also to link the unknown \mathbf{c}_e and the nodal displacement \mathbf{d}_e . Thus, the frame is defined as

$$(2.17) \quad \tilde{\mathbf{u}}(\mathbf{x}) = \begin{Bmatrix} \tilde{u}_1 \\ \tilde{u}_2 \\ \tilde{u}_3 \end{Bmatrix} = \begin{Bmatrix} \tilde{\mathbf{N}}_1 \\ \tilde{\mathbf{N}}_2 \\ \tilde{\mathbf{N}}_3 \end{Bmatrix} \mathbf{d}_e = \tilde{\mathbf{N}}_e \mathbf{d}_e, \quad (\mathbf{x} \in \Gamma_e),$$

where the symbol “ $\tilde{}$ ” is used to specify that the field is defined on the element boundary only, $\tilde{\mathbf{N}}_e$ is the matrix of shape functions, \mathbf{d}_e is the nodal displacements

of elements. Taking the surface 2-3-7-6 of a particular 8-node brick element (see Fig. 2) as an example, matrix $\tilde{\mathbf{N}}_e$ and vector \mathbf{d}_e can be expressed as

$$(2.18) \quad \tilde{\mathbf{N}}_e = [\mathbf{0} \quad \bar{\mathbf{N}}_1 \quad \bar{\mathbf{N}}_2 \quad \mathbf{0} \quad \mathbf{0} \quad \bar{\mathbf{N}}_4 \quad \bar{\mathbf{N}}_3 \quad \mathbf{0}],$$

$$(2.19) \quad \mathbf{d}_e = [u_{11} \quad u_{21} \quad u_{31} \quad u_{12} \quad u_{22} \quad u_{32} \quad \cdots \quad u_{18} \quad u_{28} \quad u_{38}]^T,$$

where the shape functions are expressed as

$$(2.20) \quad \bar{\mathbf{N}}_i = \begin{bmatrix} \tilde{N}_i & 0 & 0 \\ 0 & \tilde{N}_i & 0 \\ 0 & 0 & \tilde{N}_i \end{bmatrix}, \quad \mathbf{0} = \begin{bmatrix} 0 & 0 & 0 \\ 0 & 0 & 0 \\ 0 & 0 & 0 \end{bmatrix},$$

where \tilde{N}_i , ($i = 1, \dots, 4$) can be expressed by natural coordinate $\xi, \eta \in [-1, 1]$

$$(2.21) \quad \begin{aligned} \tilde{N}_1 &= \frac{(1+\xi)(1+\eta)}{4}, & \tilde{N}_2 &= \frac{(1-\xi)(1+\eta)}{4}, \\ \tilde{N}_3 &= \frac{(1-\xi)(1-\eta)}{4}, & \tilde{N}_4 &= \frac{(1+\xi)(1-\eta)}{4}, \end{aligned}$$

and (ξ_i, η_i) is the natural coordinate of the i -node of the element (Fig. 3).

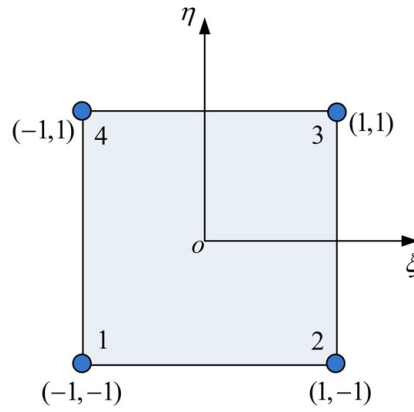


FIG. 3. Typical linear interpolation for the frame fields.

2.3. Modified functional for hybrid finite element method

The HFS-FEM formulation for 3D elastic problems can be established by the variational approach [18]. In the absence of body forces, the hybrid functional Π_{me} used for deriving the present HFS-FEM can be constructed as [15]

$$(2.22) \quad \Pi_{me} = \frac{1}{2} \iint_{\Omega_e} \sigma_{ij} \varepsilon_{ij} d\Omega - \int_{\Gamma_i} \bar{t}_i \tilde{u}_i d\Gamma + \int_{\Gamma_e} t_i (\tilde{u}_i - u_i) d\Gamma$$

where \tilde{u}_i and u_i are the intra-element displacement field defined within the element and the frame displacement field defined on the element boundary, respectively. Ω_e and Γ_e are the element domain and element boundary, respectively. Γ_t , Γ_u and Γ_I stand respectively for the specified traction boundary, specified displacement boundary and inter-element boundary ($\Gamma_e = \Gamma_t + \Gamma_u + \Gamma_I$).

Compared to the functional employed in the conventional FEM, the present hybrid functional is constructed by adding a hybrid integral term related to the intra-element and element frame displacement fields to guarantee the satisfaction of displacement and traction continuity conditions on the common boundary of two adjacent elements. By applying the Gaussian theorem, Eq. (2.22) can be simplified as

$$(2.23) \quad \begin{aligned} \Pi_{me} &= \frac{1}{2} \iint_{\Omega_e} \sigma_{ij} \varepsilon_{ij} d\Omega - \int_{\Gamma_t} \bar{t}_i \tilde{u}_i d\Gamma + \int_{\Gamma_e} t_i (\tilde{u}_i - u_i) d\Gamma \\ &= \frac{1}{2} \left(\int_{\Gamma_e} t_i u_i d\Gamma - \iint_{\Omega_e} \sigma_{ij,j} u_i d\Omega \right) - \int_{\Gamma_t} \bar{t}_i \tilde{u}_i d\Gamma + \int_{\Gamma_e} t_i (\tilde{u}_i - u_i) d\Gamma. \end{aligned}$$

Due to the satisfaction of the equilibrium equation with the constructed intra-element fields, we have the following expression for HFS finite element model

$$(2.24) \quad \begin{aligned} \Pi_{me} &= \frac{1}{2} \int_{\Gamma_e} t_i u_i d\Gamma - \int_{\Gamma_t} \bar{t}_i \tilde{u}_i d\Gamma + \int_{\Gamma_e} t_i (\tilde{u}_i - u_i) d\Gamma \\ &= -\frac{1}{2} \int_{\Gamma_e} t_i u_i d\Gamma + \int_{\Gamma_e} t_i \tilde{u}_i d\Gamma - \int_{\Gamma_t} \bar{t}_i \tilde{u}_i d\Gamma. \end{aligned}$$

The functional (2.24) contains only boundary integrals of the element and will be used to derive HFS-FEM formulation for the three-dimensional elastic problem in the following section.

2.4. Element stiffness matrix

The element stiffness equation can be generated by setting $\delta \Pi_{me} = 0$. Substituting Eqs. (2.7), (2.15) and (2.17) into the functional (2.24), we have

$$(2.25) \quad \Pi_{me} = -\frac{1}{2} \mathbf{c}_e^T \mathbf{H}_e \mathbf{c}_e + \mathbf{c}_e^T \mathbf{G}_e \mathbf{d}_e - \mathbf{d}_e^T \mathbf{g}_e,$$

where

$$(2.26) \quad \mathbf{H}_e = \int_{\Gamma_e} \mathbf{Q}_e^T \mathbf{N}_e d\Gamma, \quad \mathbf{G}_e = \int_{\Gamma_e} \mathbf{Q}_e^T \tilde{\mathbf{N}}_e d\Gamma, \quad \mathbf{g}_e = \int_{\Gamma_t} \tilde{\mathbf{N}}_e^T \bar{\mathbf{t}} d\Gamma.$$

To enforce inter-element continuity on the common element boundary, the unknown vector \mathbf{c}_e should be expressed in terms of nodal DOF \mathbf{d}_e . The stationary condition of the functional Π_{me} with respect to \mathbf{c}_e and \mathbf{d}_e yields, respectively,

$$(2.27) \quad \frac{\partial \Pi_{me}}{\partial \mathbf{c}_e^T} = -\mathbf{H}_e \mathbf{c}_e + \mathbf{G}_e \mathbf{d}_e = \mathbf{0},$$

$$(2.28) \quad \frac{\partial \Pi_{me}}{\partial \mathbf{d}_e^T} = \mathbf{G}_e^T \mathbf{c}_e - \mathbf{g}_e = \mathbf{0}.$$

Therefore, the relationship between \mathbf{c}_e and \mathbf{d}_e , and the stiffness equation can be obtained as follows

$$(2.29) \quad \mathbf{c}_e = \mathbf{H}_e^{-1} \mathbf{G}_e \mathbf{d}_e,$$

$$(2.30) \quad \mathbf{K}_e \mathbf{d}_e = \mathbf{g}_e,$$

where $\mathbf{K}_e = \mathbf{G}_e^T \mathbf{H}_e^{-1} \mathbf{G}_e$ is the element stiffness matrix. It should be mentioned that the condition number of matrix \mathbf{H}_e may become very large if the positions of source points are not chosen appropriately. This issue can be determined by numerical experiments for the parameter γ in Eq. (2.11). According to our experience, the suitable range for γ is between 2 and 15 to assure a better condition number for matrix \mathbf{H}_e in order to improve the accuracy.

2.5. Numerical integral over element

Generally, it is difficult to get the analytical expression of the integral in Eq.(2.26) and numerical integration over the element is required. In our calculation the widely used Gaussian integration is employed.

Consider a surface of the 3D hexahedron element, as shown in Fig. 3, the vector normal to the surface can be obtained by

$$(2.31) \quad \mathbf{v}_n = \mathbf{v}_\xi \times \mathbf{v}_\eta = \begin{Bmatrix} v_{nx} \\ v_{ny} \\ v_{nz} \end{Bmatrix} = \begin{Bmatrix} \frac{dx}{d\xi} \\ \frac{dy}{d\xi} \\ \frac{dz}{d\xi} \end{Bmatrix} \times \begin{Bmatrix} \frac{dx}{d\eta} \\ \frac{dy}{d\eta} \\ \frac{dz}{d\eta} \end{Bmatrix} = \begin{Bmatrix} \frac{dy}{d\xi} \frac{dz}{d\eta} - \frac{dy}{d\eta} \frac{dz}{d\xi} \\ \frac{dz}{d\xi} \frac{dx}{d\eta} - \frac{dz}{d\eta} \frac{dx}{d\xi} \\ \frac{dx}{d\xi} \frac{dy}{d\eta} - \frac{dx}{d\eta} \frac{dy}{d\xi} \end{Bmatrix},$$

where \mathbf{v}_ξ and \mathbf{v}_η are the tangential vectors in the ξ -direction and η -direction, respectively, calculated by

$$(2.32) \quad \mathbf{v}_\xi = \begin{pmatrix} \frac{dx}{d\xi} \\ \frac{dy}{d\xi} \\ \frac{dz}{d\xi} \end{pmatrix} = \sum_{i=1}^{n_d} \frac{\partial N_i(\xi, \eta)}{\partial \xi} \begin{pmatrix} x_i \\ y_i \\ z_i \end{pmatrix},$$

$$\mathbf{v}_\eta = \begin{pmatrix} \frac{dx}{d\eta} \\ \frac{dy}{d\eta} \\ \frac{dz}{d\eta} \end{pmatrix} = \sum_{i=1}^{n_d} \frac{\partial N_i(\xi, \eta)}{\partial \eta} \begin{pmatrix} x_i \\ y_i \\ z_i \end{pmatrix},$$

where n_d is the number of nodes of the surface, (x_i, y_i, z_i) are the nodal coordinates. Thus the unit normal vector is given by

$$(2.33) \quad \mathbf{n} = \frac{\mathbf{v}_n}{|\mathbf{v}_n|},$$

where

$$(2.34) \quad J(\xi, \eta) = |\mathbf{v}_n| = \sqrt{v_{nx}^2 + v_{ny}^2 + v_{nz}^2}$$

is the Jacobian of the transformation from Cartesian coordinates (x, y) to natural coordinates (ξ, η) .

For the \mathbf{H} matrix, we introduce the matrix function

$$(2.35) \quad \mathbf{F}(\mathbf{x}, \mathbf{y}) = [F_{ij}(x, y)]_{m \times m} = \mathbf{Q}_e^T \mathbf{N}_e.$$

Then we can get

$$(2.36) \quad \mathbf{H}_e = \int_{\Gamma_e} \mathbf{Q}_e^T \mathbf{N}_e d\Gamma = \int_{\Gamma_e} \mathbf{F}(\mathbf{x}, \mathbf{y}) d\Gamma,$$

and we rewrite it to the component form as

$$(2.37) \quad H_{ij} = \int_{\Gamma_e} F_{ij}(x, y) dS = \sum_{l=1}^{n_f} \int_{\Gamma_{el}} F_{ij}(x, y) dS.$$

Using the relationship

$$(2.38) \quad dS = J(\xi, \eta) d\xi d\eta$$

and the Gaussian numerical integration, we can obtain

$$(2.39) \quad H_{ij} = \sum_{l=1}^{n_f} \int_{-1}^1 F_{ij}[x(\xi, \eta), y(\xi, \eta)] J(\xi, \eta) d\xi d\eta \\ \approx \sum_{l=1}^{n_f} \left\{ \sum_{s=1}^{n_p} \sum_{t=1}^{n_p} w_s w_t F_{ij}[x(\xi_s, \eta_t), y(\xi_s, \eta_t)] J(\xi_s, \eta_t) \right\},$$

where n_f and n_p are respectively the number of surface of the 3D element and the number of Gaussian integral points in each direction of the element surface. Similarly, we can calculate the \mathbf{G}_e matrix by

$$(2.40) \quad G_{ij} = \sum_{l=1}^{n_f} \int_{-1}^1 \tilde{F}_{ij}[x(\xi, \eta), y(\xi, \eta)] J(\xi, \eta) d\xi d\eta \\ \approx \sum_{l=1}^{n_f} \left\{ \sum_{s=1}^{n_p} \sum_{t=1}^{n_p} w_s w_t \tilde{F}_{ij}[x(\xi_s, \eta_t), y(\xi_s, \eta_t)] J(\xi_s, \eta_t) \right\}.$$

It should be mentioned that the calculation of vector \mathbf{g}_e in Eq. (2.30) is the same as that in the conventional FEM, so it is convenient to incorporate the proposed HFS-FEM into the standard FEM program. Besides, the stress and traction estimations are directly computed from Eqs. (2.12) and (2.13), respectively. The boundary displacements can be directly computed from Eq. (2.17) while the displacements at interior points of the element can be determined from Eq. (2.7) plus the recovered rigid-body modes in each element, which will be introduced in the following section.

2.6. Recovery of rigid-body motion terms

From the above procedures, we can see that the solution will fail if any of the functions u_{ij}^* is in a rigid body motion mode due to that the matrix \mathbf{H}_e is not in full rank and becomes singular for inversion [14]. Therefore, special care should be taken to discard all rigid body motion terms from \mathbf{u}_e to prevent the element deformability matrix \mathbf{H}_e from being singular. However, it is necessary to reintroduce the discarded rigid-body motion terms when calculating the internal field \mathbf{u}_e of an element. For this purpose the least squares method can be employed. The missing terms can easily be recovered by setting for the augmented internal field

$$(2.41) \quad \mathbf{u}_e = \mathbf{N}_e \mathbf{c}_e + \begin{bmatrix} 1 & 0 & 0 & 0 & x_3 & -x_2 \\ 0 & 1 & 0 & -x_3 & 0 & x_1 \\ 0 & 0 & 1 & x_2 & -x_1 & 0 \end{bmatrix} \mathbf{c}_0$$

and using a least-square procedure to match u_{eh} and \tilde{u}_{eh} at the nodes of the element boundary

$$(2.42) \quad \min = \sum_{i=1}^n [(u_{1i} - \tilde{u}_{1i})^2 + (u_{2i} - \tilde{u}_{2i})^2 + (u_{3i} - \tilde{u}_{3i})^2],$$

where n is the number of nodes for the element under consideration. The above equation finally yields

$$(2.43) \quad \mathbf{c}_0 = \mathbf{R}_e^{-1} \mathbf{r}_e$$

where

$$(2.44) \quad \mathbf{R}_e = \sum_{i=1}^n \begin{bmatrix} 1 & 0 & 0 & 0 & x_{3i} & -x_{2i} \\ 0 & 1 & 0 & -x_{3i} & 0 & x_{1i} \\ 0 & 0 & 1 & x_{2i} & -x_{1i} & 0 \\ 0 & -x_{3i} & x_{2i} & x_{2i}^2 + x_{3i}^2 & -x_{1i}x_{2i} & -x_{1i}x_{3i} \\ x_{3i} & 0 & -x_{1i} & -x_{1i}x_{2i} & x_{1i}^2 + x_{3i}^2 & -x_{2i}x_{3i} \\ -x_{2i} & x_{1i} & 0 & -x_{1i}x_{3i} & -x_{2i}x_{3i} & x_{1i}^2 + x_{2i}^2 \end{bmatrix},$$

$$(2.45) \quad \mathbf{r}_e = \sum_{i=1}^n \begin{bmatrix} \Delta u_{e1i} \\ \Delta u_{e2i} \\ \Delta u_{e3i} \\ \Delta u_{e3i}x_{2i} - \Delta u_{e2i}x_{3i} \\ \Delta u_{e1i}x_{3i} - \Delta u_{e3i}x_{1i} \\ \Delta u_{e2i}x_{1i} - \Delta u_{e1i}x_{2i} \end{bmatrix}.$$

3. Formulations of the HFS-FEM for 3D elasticity with body force

3.1. Governing equations

Consider the three-dimensional isotropic body occupying the domain Ω , as shown in Fig. 1, the equilibrium equation for the body with body force b_i can be expressed as

$$(3.1) \quad \sigma_{ij,j} = -b_i \quad i, j = 1, 2, 3.$$

The constitutive equations and the generalized kinematical relation are the same as those in Eqs. (2.2) and (2.3). Therefore, the equilibrium equations (3.1) can be rewritten in terms of displacements as

$$(3.2) \quad Gu_{i,jj} + \frac{G}{1-2\nu}u_{j,ji} = -b_i.$$

For a well-posed boundary value problem, boundary conditions are also defined by Eqs. (2.5) and (2.6). In the following parts, we will present the procedure for handling the body force appearing in Eq. (3.2).

3.2. The method of particular solution

The inhomogeneous term b_i associated with the body force in Eq. (3.2) can be effectively handled by means of the method of particular solution presented in [15, 23]. In this approach, the displacement u_i is decomposed into two parts, a homogeneous solution u_i^h and a particular solution u_i^p

$$(3.3) \quad u_i = u_i^c + u_i^p,$$

where the particular solution u_i^p should satisfy the governing equation

$$(3.4) \quad Gu_{i,jj}^p + \frac{G}{1-2\nu} u_{j,ji}^p = -b_i$$

without any restriction of boundary condition. However, the homogeneous solution should satisfy

$$(3.5) \quad Gu_{i,jj}^h + \frac{G}{1-2\nu} u_{j,ji}^h = 0$$

with the modified boundary conditions

$$(3.6) \quad u_i^h = \bar{u}_i - u_i^p \quad \text{on } \Gamma_u,$$

$$(3.7) \quad t_i^h = \bar{t}_i - t_i^p \quad \text{on } \Gamma_t.$$

From above equations it can be seen that once the particular solution u_i^p is known, the homogeneous solution u_i^h in Eqs. (3.5)–(3.7) can be obtained using HFS-FEM. The final solution can then be given by Eq. (3.3). In the next section, radial basis function approximation will be introduced to obtain the particular solution, and the HFS-FEM will be used for solving Eqs. (3.5)–(3.7).

3.3. Radial basis function approximation

For the body force b_i , it is generally impossible to find an analytical solution which enable us to convert the domain integral into a boundary one. So we must approximate it by a combination of basis (trial) functions or other methods. Radial basis function (RBF), which has been found to be most suitable for this purpose [24, 25], is used for interpolation of body forces in this paper. Hence, we assume

$$(3.8) \quad b_i \approx \sum_{j=1}^N \alpha_i^j \varphi^j,$$

where N is the number of interpolation points, φ^j are the RBFs and α_i^j are the coefficients to be determined. Subsequently, the particular solution can be approximated by

$$(3.9) \quad u_i^p = \sum_{j=1}^N \alpha_i^j \Phi_{ik}^j,$$

where Φ_{ik}^j is the approximated particular solution kernel of displacement. Once the basis functions are selected, the problem of finding a particular solution is reduced to solve the following equation

$$(3.10) \quad G\Phi_{il,kk} + \frac{G}{1-2\nu}\Phi_{kl,ki} = -\delta_{il}\varphi.$$

To solve this equation, the displacement is expressed in terms of the Galerkin–Papkovich vectors

$$(3.11) \quad \Phi_{ik} = \frac{1-\nu}{G}F_{ik,mm} - \frac{1}{2G}F_{mk,mi}.$$

Substituting Eq. (3.11) into Eq. (3.10), we can obtain the following bi-harmonic equation

$$(3.12) \quad \nabla^4 F_{il} = -\frac{1}{1-\nu}\delta_{il}\varphi.$$

Taking the Spline Type RBF $\varphi = r^{2n-1}$ as an example, we have following solutions

$$(3.13) \quad F_{li} = -\frac{\delta_{li}}{1-\nu} \frac{r^{2n+3}}{(2n+1)(2n+2)(2n+3)(2n+4)},$$

$$(3.14) \quad \Phi_{li} = A_0(A_1\delta_{li} + A_2r_{,i}r_{,l}),$$

where

$$(3.15) \quad \begin{aligned} A_0 &= -\frac{1}{8G(1-\nu)} \frac{r^{2n+1}}{(n+1)(n+2)(2n+1)}, \\ A_1 &= 7 + 4n - 4v(n+2), \\ A_2 &= -(2n+1), \end{aligned}$$

and r_j represents the Euclidean distance between a field point (x, y, z) and a given point (x_j, y_j, z_j) in the domain of interest. The corresponding particular solution of stresses can be obtained by

$$(3.16) \quad S_{lij} = G(\Phi_{li,j} + \Phi_{lj,i}) + \lambda\delta_{ij}\Phi_{lk,k},$$

where $\lambda = \frac{2\nu}{1-2\nu}G$. Substituting Eq. (3.14) into Eq. (3.16), we have

$$(3.17) \quad S_{lij} = B_0\{B_1(r_{,j}\delta_{li} + r_{,i}\delta_{jl}) + B_2\delta_{ij}r_{,l} + B_3r_{,i}r_{,j}r_{,l}\},$$

where

$$\begin{aligned}
 (3.18) \quad B_0 &= -\frac{1}{4(1-v)} \frac{r^{2n}}{(n+1)(n+2)}, \\
 B_1 &= 3 + 2n - 2v(n+2), \\
 B_2 &= 2v(n+2) - 1, \\
 B_3 &= 1 - 2n.
 \end{aligned}$$

3.4. HFS-FEM for homogeneous solution

After obtaining the particular solution, next step is to modify boundary conditions using Eqs. (3.6) and (3.7), then we can treat the 3D problem as a homogeneous problem governed by Eqs. (3.5)–(3.7) by using the HFS-FEM presented in Section 2. It is clear that once the particular and homogeneous solutions for displacement and stress components at nodal points are determined, the distribution of displacement and stress fields at any point in the domain can be calculated using the element interpolation function.

4. Numerical examples

The performance of the proposed 3D HFS-FEM is now evaluated with a number of challenging problems from the literature. First, the 3D patch test presented in [26] is conducted for the proposed element. Then the standard two-element distortion test and straight beam tests (with Rectangular, Trapezoid and Parallelogram shape elements) are conducted. An irregularly meshed bi-material beam is also investigated and the element performance of different elements is compared. After that, a cube under uniform loading and body force are presented to demonstrate the performance of the method for solving problems involving body forces. Then a perforated thick plate is considered for assess the performance in handling stress concentration. Finally, nearly incompressible materials are investigated to applicability to volumetric locking problems.

EXAMPLE 1. 3D Patch test. A standard 3D patch test presented by MACNEAL and HARDER [26] is carried out in this example. A unit cube is discretized by seven irregular 8-node hexahedral elements, as shown in Fig. 4. The material is linear elastic with Young's module $E = 10^6$ Pa and Poisson ratio $\nu = 0.25$. The eight exterior nodes are given a prescribed linear displacement shown in Eq. (4.1) to reproduce a uniform strain/stress state for the irregular elements.

$$\begin{aligned}
 (4.1) \quad u &= 0.5 \times 10^{-3}(2x + y + z), \\
 v &= 0.5 \times 10^{-3}(x + 2y + z), \\
 w &= 0.5 \times 10^{-3}(x + y + 2z).
 \end{aligned}$$

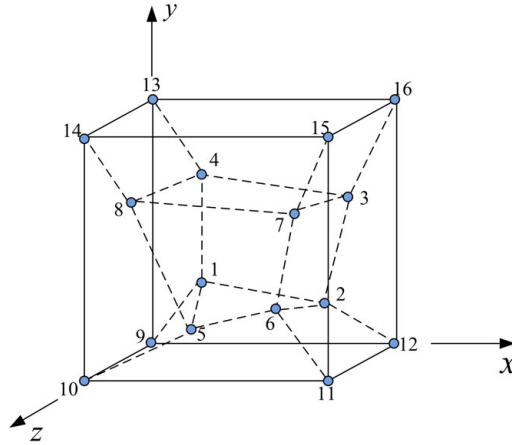


FIG. 4. 3D patch test with wrap element (unit cube, $E = 10^6$, $\nu = 0.25$).

Table 1 gives the nodal coordinates of the elements and the boundary condition for the external eight nodes, and the interior nodes are free of any external load. It is found that both the 8-node and 20-node brick element can successfully pass the patch test with good marks described in MACNEAL and HARDER [26]. It is demonstrated that the linear field can be approximated by the superposition of finite number of the fundamental solutions with relatively high accuracy.

Table 1. Node coordinates and displacement boundary condition for external nodes of the 3D patch test.

Node	Coordinates			Displacement B.C.		
	x_1	x_2	x_3	u_1	u_2	u_3
1	0.249	0.342	0.342	–	–	–
2	0.826	0.288	0.288	–	–	–
3	0.850	0.649	0.263	–	–	–
4	0.273	0.750	0.230	–	–	–
5	0.320	0.186	0.643	–	–	–
6	0.677	0.305	0.683	–	–	–
7	0.788	0.693	0.644	–	–	–
8	0.165	0.745	0.702	–	–	–
9	0.0	0.0	0.0	0.0	0.0	0.0
10	1.0	0.0	0.0	1.0	0.5	0.5
11	1.0	1.0	0.0	1.5	1.5	1.0
12	0.0	1.0	0.0	0.5	1.0	0.5
13	0.0	0.0	1.0	0.5	0.5	1.0
14	1.0	0.0	1.0	1.5	1.0	1.5
15	1.0	1.0	1.0	2.0	2.0	2.0
16	0.0	1.0	1.0	1.0	1.5	1.5

EXAMPLE 2. *Beam bending: sensitivity to mesh distortion.* In order to demonstrate the sensibility of the proposed model to mesh distortion, the well-known two-element distortion test is examined [27–30], as shown in Fig. 5. The surface separating the two elements is gradually rotated to skew the mesh. The tip deflection at point A of the beam under pure bending is presented in Fig. 6. From this figure, it can be seen that the error of deflection from HFS-FEM (HFS-HEX8) increases from 10% to about 40% when the distortion parameter Δ increases from 1 to 4. However, the present element is not so sensitive to the distortion as the elements by PIAN and TONG [31] and WEISSMAN [30]. Comparing with those obtained by PIAN and TONG [31] and WEISSMAN [30], it is obvious that the present results are much better when the element is distorted.

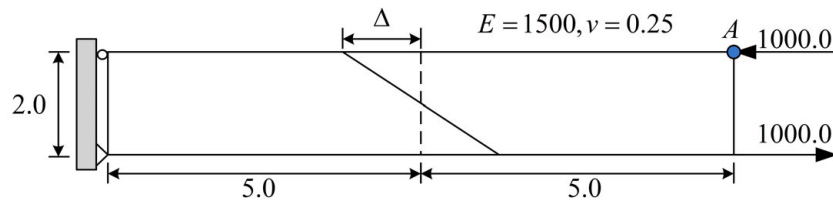


FIG. 5. Perspective view of a cantilever beam under end moment: sensitivity to mesh distortion.

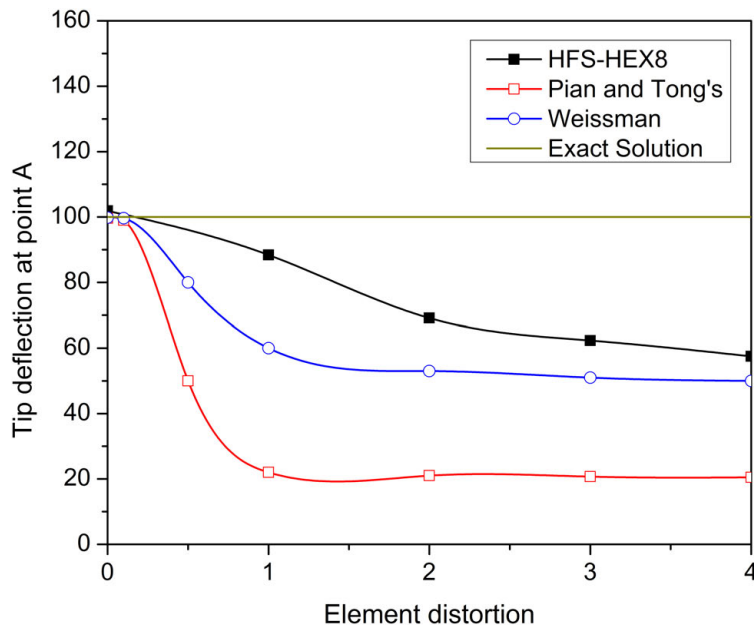


FIG. 6. Comparison of deflection at point A for a cantilever beam; deflection at point A from a cantilever beam under end moment.

EXAMPLE 3. *Cantilever beam under shear loading.* A set of beams with rectangular, trapezoidal and parallelogram shapes [26, 32] as shown in Fig. 7 are investigated. The materials constants are $E = 1.0 \times 10^7$ and $\nu = 0.3$. One end of the beam is fixed and the other end of the beam is applied a concentrated load of $P = 1$. The length, width and thickness of the beams are 6.0, 0.2 and 0.1, respectively. The obtained results are normalized by the theoretical solution, 0.1081, which is obtained from the beam theory [26].

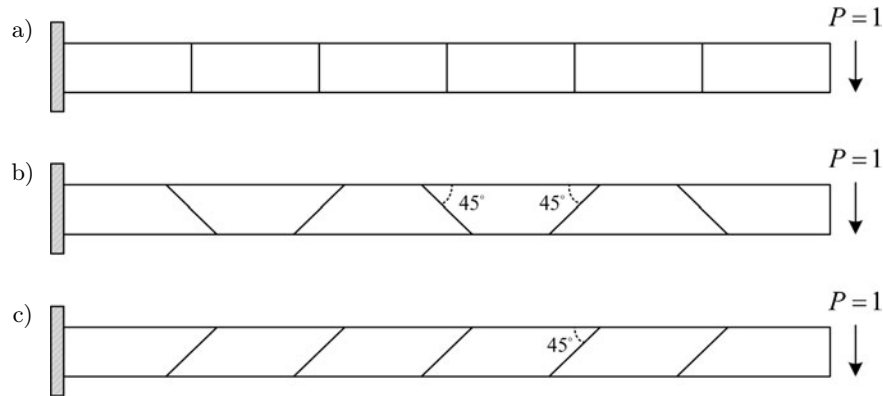


FIG. 7. Perspective views of straight cantilever beams: a) regular shape beam, b) trapezoid shape elements, c) parallelogram shape element.

The normalized results are shown in Table 2. It can be found that the HFS-HEX8 element cannot overcome the locking phenomenon for the trapezoidal case and parallelogram case. It exhibits severely locking for the trapezoidal case, which is only 0.281 times of the exact value. However, it still gives better performance compared with the results produced by the elements of Pian and Tong. For the parallelogram case, the accuracy of the HFS-HEX8 element is similar with those of element by CAO *et al.* [32] and PIAN and TONG [31].

Table 2. Comparison of normalized tip deflections of straight beam in load direction.

Mesh type	Pian and Tong [31]	Cao <i>et. al.</i> [32]	HFS-HEX-8
Rectangular	0.981	0.981	0.962
Trapezoidal	0.047	0.980	0.281
Parallelogram	0.625	0.653	0.657

EXAMPLE 4. *Irregularly meshed beam with two materials.* In the fourth example, a long beam composed of two materials as shown in Fig. 8 is investigated. The beam is 4m long with a constant squared cross-section of $0.5 \times 0.5 \text{ m}^2$.

The material parameters are respectively $E_1 = 200$ MPa, $\nu_1 = 0.3$ and $E_2 = 400$ MPa, $\nu_2 = 0.3$ [33]. The interface between the two materials is considered perfectly bonded. The displacements are restrained on one end of the beam and a transversal force of 2 kN is uniformly applied on the cross-section of the other end, as shown in Fig. 8.

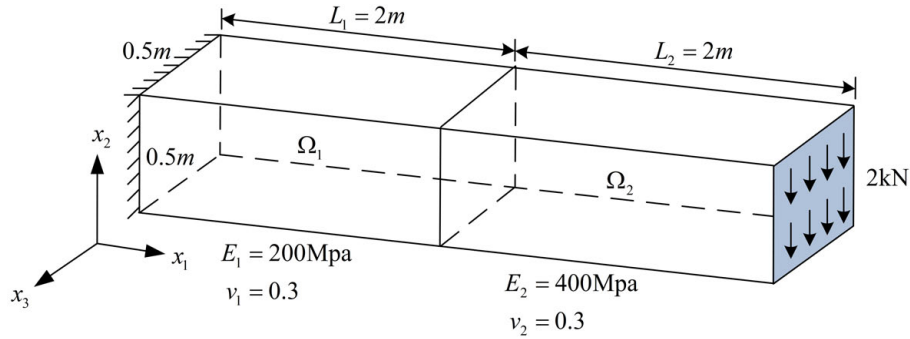


FIG. 8. Irregularly meshed bimaterial beam: geometry, materials and boundary conditions.

The response of the beam has been computed using the 3D HFS-FEM for three irregular meshes, as shown in Fig. 9: i.e., Mesh 1 ($2 \times 2 \times 10$ elements with 99 nodes), Mesh 2 ($4 \times 4 \times 20$ elements with 525 nodes) and Mesh 3 ($8 \times 8 \times 40$ elements with 3321 nodes). The transverse displacement u_2 along the force direction at the central tip point of the cross-section is used for comparison. Table 3 gives the transverse displacement u_2 obtained by the HFS-FEM using HFS-HEX8 and HFS-HEX20 elements as well as the results by ABAQUS C3D8 elements and enhanced strain elements (EAS) [34]. It is found that the C3D8 element is severely locked as expected for Mesh 1. EAS elements give much better results than the original C3D8 elements. The HFS-HEX8 element also displays the locking problem for Mesh 1 but significantly improved the results of C3D8, which has the similar performance to EAS element. The quadratic element HFS-HEX20 has the best performance in the listed elements. However, it can be expected that all the elements both from HFS-FEM and ABAQUS will converge to the benchmark value of 3.8388 cm (obtained by ABAQUS using $20 \times 20 \times 20$ elements with 71001 nodes shown in Fig. 10) with the increasing of the mesh density.

Comparison with the solution of ABAQUS using several ten thousands of nodes, it is interesting that similar results with nearly same accuracy can be obtained by HFS-FEM using much less meshes. It is expected that using non-uniform mesh density for the interface and ends, similar results are obtainable with an even smaller number of elements. It can be concluded from Table 3 that the HFS-FEM with linear or quadratic elements are not sensitive to element

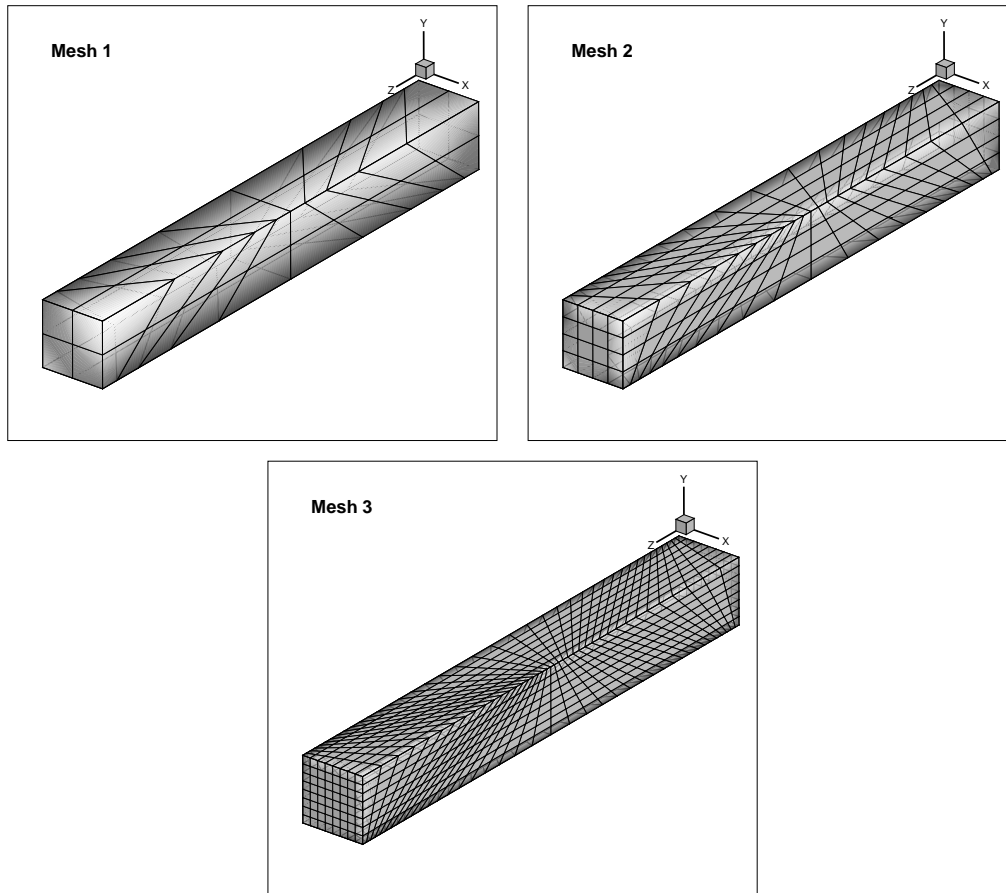


FIG. 9. Irregularly meshed bimaterial beam: Mesh 1 ($2 \times 2 \times 10$ elements), Mesh 2 ($4 \times 4 \times 20$ elements) and Mesh 3 ($8 \times 8 \times 40$ elements).

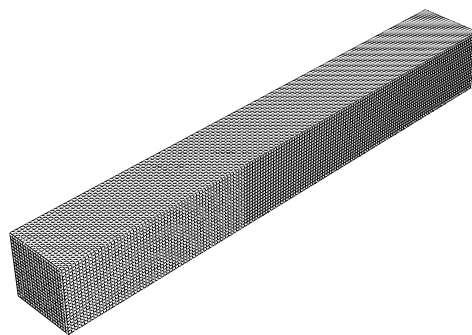


FIG. 10. Regularly meshed bimaterial beam: fine mesh used by ABAQUS for benchmark reference ($20 \times 20 \times 100$ elements).

distortion as shown in Example 2, and the shear locking problems is not as severe as C3D8 and has competitive performance with the EAS.

Table 3. Transversal displacement and relative errors of the irregularly meshed beam calculated by HFS-FEM and ABAQUS using different elements.

Mesh	HFS-FEM		ABAQUS	
	HEX8	HEX20	EAS	C3D8
Mesh 1 ($2 \times 2 \times 10$)	3.0842 (19.65%)	3.7890 (1.30%)	3.2541 (15.23%)	2.1612 (43.70%)
Mesh 2 ($4 \times 4 \times 20$)	3.6188 (5.73%)	3.8305 (0.22%)	3.6982 (3.66%)	3.2769 (14.64%)
Mesh 3 ($8 \times 8 \times 40$)	3.7650 (1.92%)	3.8382 (0.01%)	3.7993 (1.03%)	3.6878 (3.93%)

Note: displacement unit: cm; values in the parentheses are the relative error.

EXAMPLE 5. *Cubic block under uniform tension and body force.* To investigate the performance of the proposed method for problems involving body forces, an isotropic cubic block subject to a uniform tension is considered in this example. The dimension of the block is $10 \times 10 \times 10$ and its geometry and boundary conditions are shown in Fig. 11. A constant body force of 10 Mpa and uniform distributed tension of 100 MPa are applied to the cube. Three different meshes with distorted 8-node brick elements: Mesh 1 ($4 \times 4 \times 4$), Mesh 2 ($6 \times 6 \times 6$) and Mesh 3 ($10 \times 10 \times 10$) as shown in Fig. 12, are employed to investigate the convergence of the method. The displacement and stress at Point A calculated

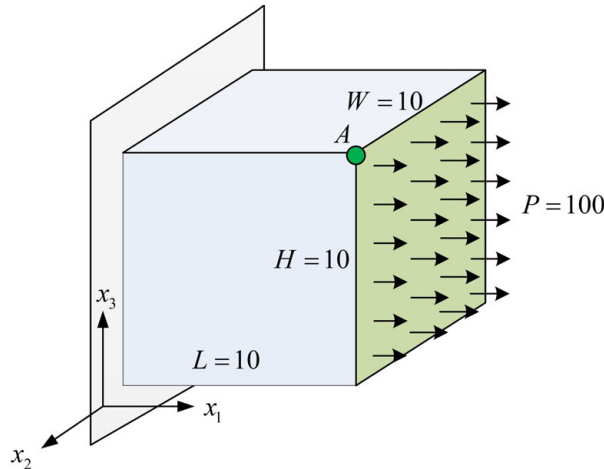


FIG. 11. Cubic block under uniform tension and body force: geometry, boundary condition and loading.

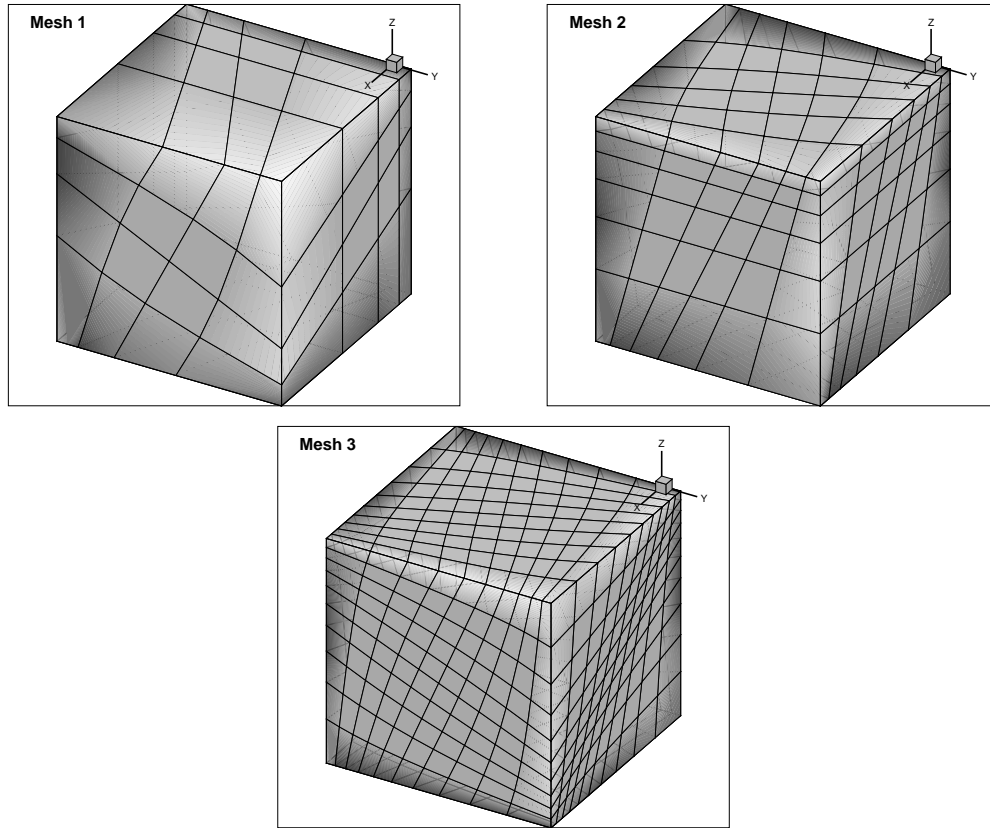


FIG. 12. Cubic block under uniform tension and body force: Mesh 1 ($4 \times 4 \times 4$ elements), Mesh 2 ($6 \times 6 \times 6$ elements) and Mesh 3 ($10 \times 10 \times 10$ elements).

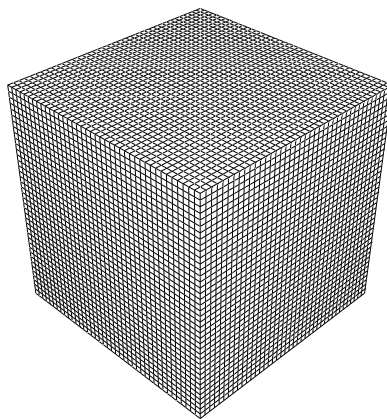


FIG. 13. Cubic block under uniform tension and body force: fine mesh used by ABAQUS for benchmark reference ($40 \times 40 \times 40$ elements).

by ABAQUS with a very fine mesh (shown in Fig. 13, $40 \times 40 \times 40$ C3D8 element with 68921 nodes) are given as a reference benchmark for comparison, which can be viewed as the exact solution.

Figures 14 and 15 present the displacement component u_1 and the stress component σ_{11} at Point A of the block, which are calculated by the HFS-FEM on the three meshes shown in Fig. 12. The results from C3D8 and EAS elements

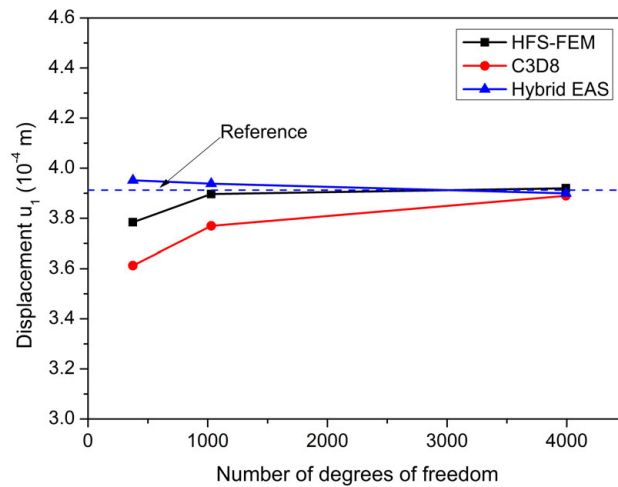


FIG. 14. Cubic block with body force under uniform distributed load: convergent study of displacements.

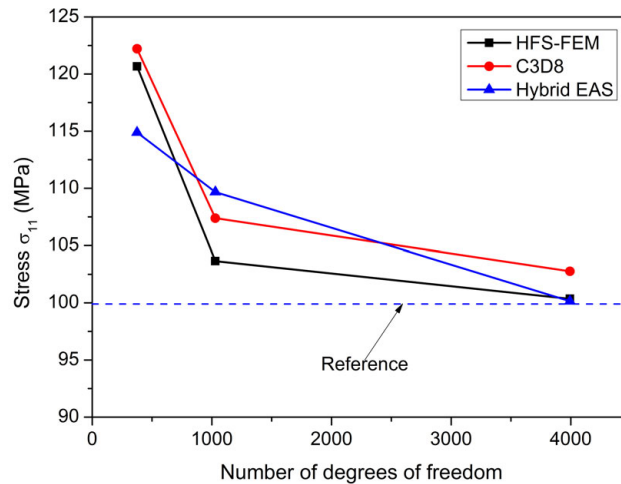


FIG. 15. Cubic block with body force under uniform distributed load: convergent study of stresses.

are also presented for comparison. It can be seen from these figures that the results obtained both from HFS-FEM and ABAQUS converge to the benchmark value with the increasing of the number of degree of freedom (DOF). For Mesh 1, the hybrid EAS element has the best performance while for Mesh 2 and Mesh 3 it can be seen that HFS-FEM with HEX8 elements exhibits better accuracy for both displacement and stresses compare with EAS in traditional FEM. From the results it can be seen that the C3D8 has the worst performance in the presented three type elements. Contour plots of u_1 and σ_{11} obtained by HFS-FEM on Mesh 3 are also presented in Fig. 16.

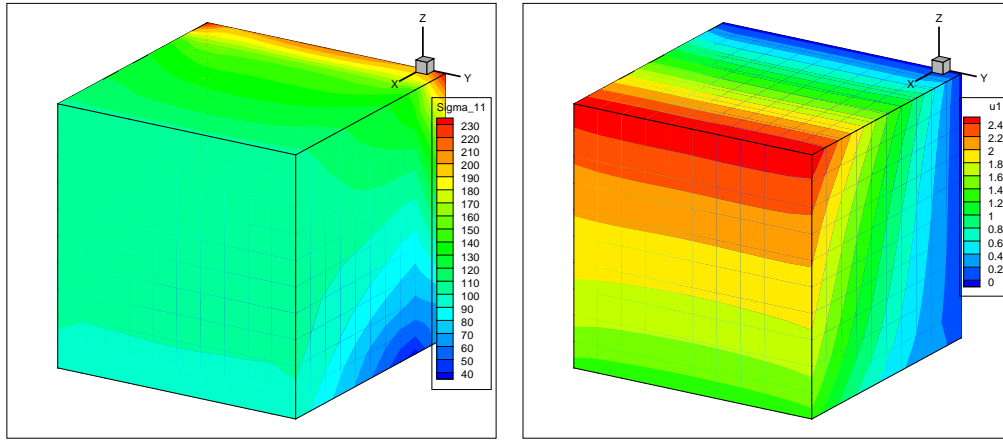


FIG. 16. Contour plots of displacement u_1 and stress σ_{11} of the cube.

It should be noted that for problems involving body forces the accuracy of the RBF interpolation has to be considered for a satisfactory solution. Due to our current method for producing the interpolation points, i.e. the interpolation points are the same as the element nodes, thus increasing the nodes of the domain will improve the accuracy for body force approximation, and then the results of displacement and stress are improved. Thus, it is expected to increase the number of nodes so as to increase the interpolation points for improving the accuracy of HFS-FEM for problems involving body force. The details on the RBF interpolation can be found in previous literatures [10, 35, 36].

EXAMPLE 6. Thick plate with a centered hole. The influence of holes on the distribution of stresses in structural elements has been investigated for a long time [37–39]. To demonstrate the capability of the new method for handling complex geometry and stress concentration, one thick plate with a circle hole at its center is investigated in this example. A uniform displacement $u_1 = 1$ mm is applied on one face of the plate along x axis as shown in Fig. 17. The reference results are obtained by ABAQUS using 138,866 C3D8R elements with 151,725

nodes as shown in Fig. 18. Three different meshes used in this example, Mesh 1 (660 elements with 985 nodes), Mesh 2 (1392 elements with 1876 nodes) and Mesh 3 (5274 elements with 6657 nodes), are shown in Fig. 19.

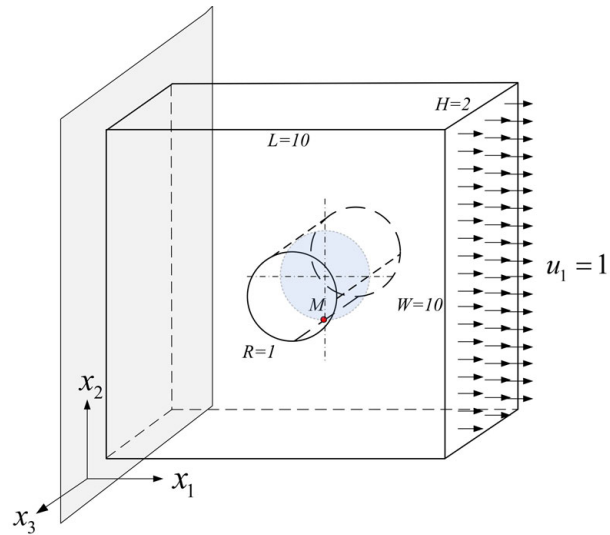


FIG. 17. Thick plate with central hole: geometry, material and boundary conditions.

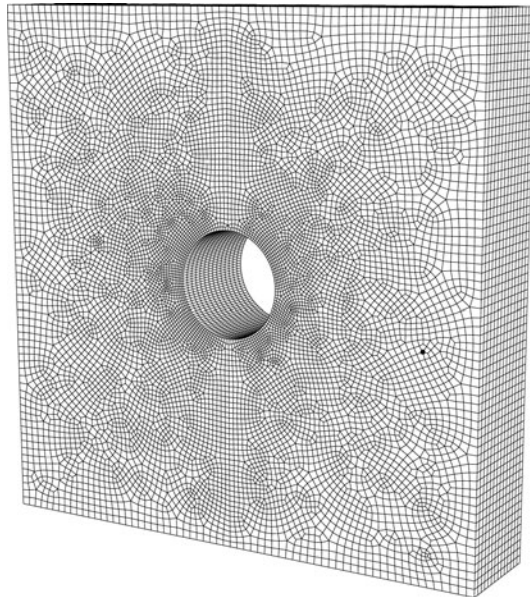


FIG. 18. Thick plate with central hole: fine mesh used by ABAQUS for benchmark reference (138866 elements with 151725 nodes).

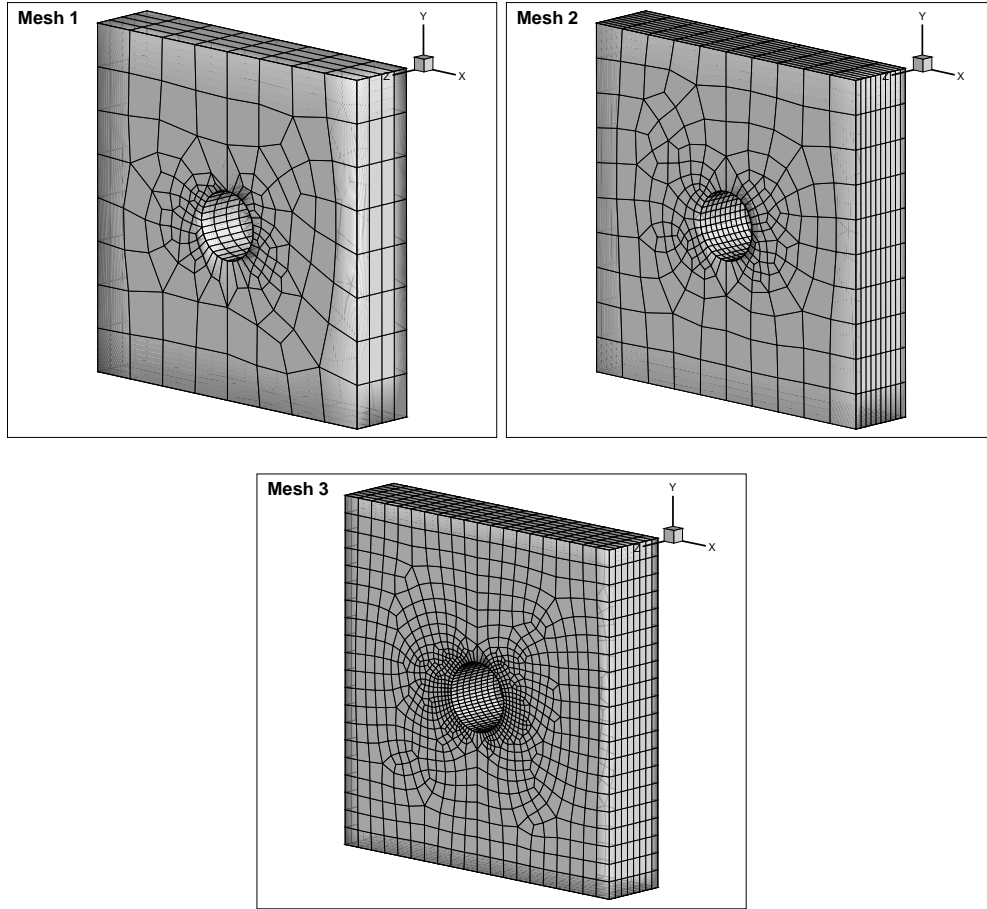


FIG. 19. Perforated thick plate: Mesh 1 (660 elements with 985 nodes), Mesh 2 (1392 elements with 1876 nodes) and Mesh 3 (5274 elements with 6657 nodes).

Figure 20 presents the results calculated by the HFS-FEM and ABAQUS for the stress at point M (as shown in Fig. 17). It is obvious that the results from HFS-FEM are much better than those given by ABAQUS. The error of HFS-FEM is less than 3% while the error of ABAQUS is larger than 20% by using the finer Mesh 3. The von Mises stress of the thick plates is also given in Fig. 21, in which the von Mises stress is given by

$$(4.2) \quad \sigma_{vm} = \sqrt{\frac{3}{2} \sigma'_{ij} \sigma'_{ji}},$$

where σ_{vm} is the von Mises stress, σ_{ij} is the stress tensor and σ'_{ij} is the deviatoric

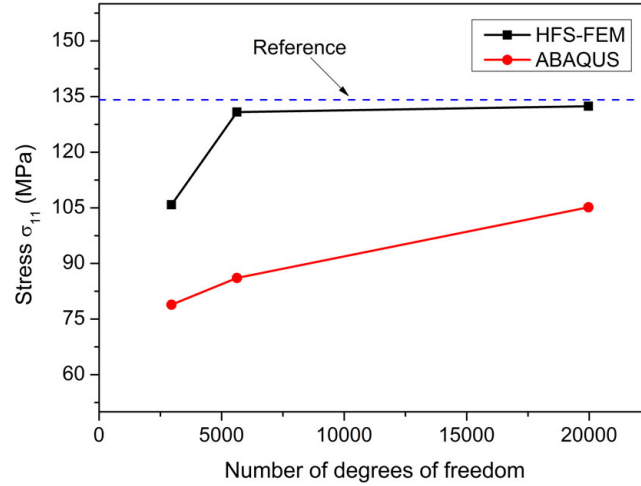


FIG. 20. Perforated thick plate under uniform distributed load: convergent study of stresses.

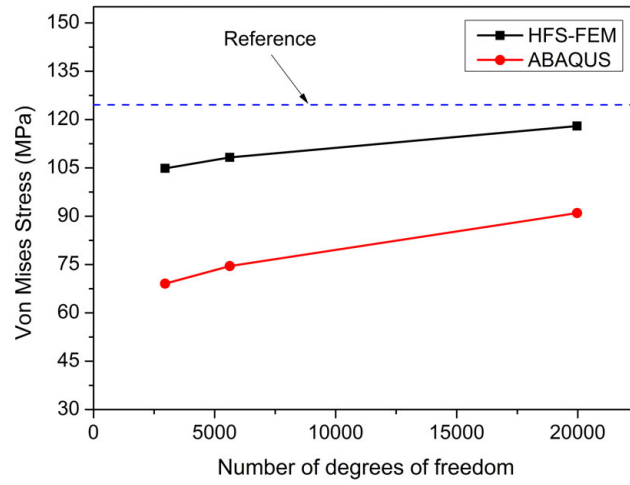


FIG. 21. Perforated thick plate under uniform distributed load: convergent study of Von Mises stress.

stress defined by

$$(4.3) \quad \sigma'_{ij} = \sigma_{ij} - \frac{1}{3} \sigma_{kk} \delta_{ij}.$$

It can be seen from Fig. 21 that the HFS-FEM demonstrates a promising performance with far smaller error than that from ABAQUS in the stress concentration problems.

EXAMPLE 7. *Nearly incompressible block* [28, 40]. As shown in Fig. 22, a nearly incompressible block with dimensions $100 \times 100 \times 50$ is considered. The block is fixed at the bottom and loaded at the top by a uniform pressure of $q = 250$ /unit area, acting on an area of 20×20 at the center. Due to symmetry of the problem, only a quarter of the block is discretized with a uniform $5 \times 5 \times 5$ mesh. The bottom face of the block is fixed in the x_3 -direction, and the symmetry boundary conditions are applied to the symmetry surface of the block. The geometry and the material properties as well as the load applied and the boundary conditions are given in Fig. 22.

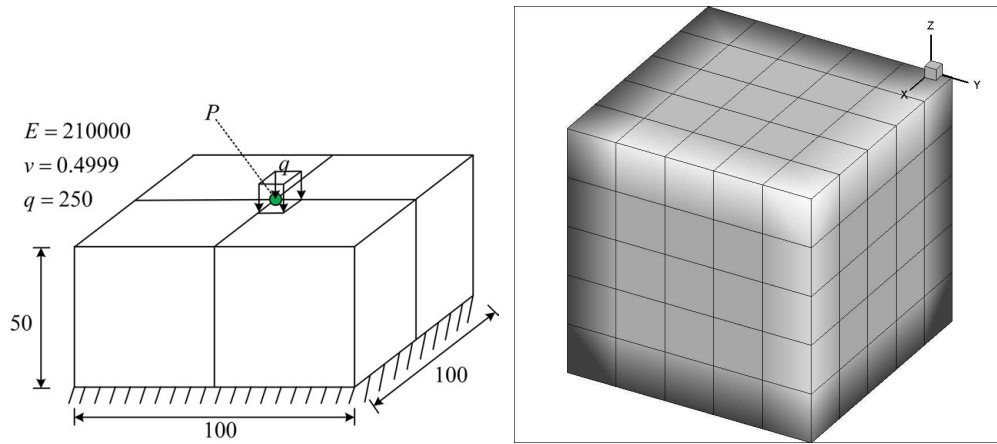


FIG. 22. Nearly incompressible block: geometry, boundary conditions and the tested mesh.

The vertical displacement at the top center P of the block is listed for the HFS-HEX8 element, HIS element [41] as well as the 3D.EAS-30 [28] and QM1/E12 [42] element in Table 4. It is found that HFS-HEX8 is free of volumetric locking and shows a significantly softer response compared with the QM1/E12 element. The enhanced strain element 3D.EAS-30 exhibits a little stiffer than HFS-HEX-8 and HIS proposed by AREIAS *et al.* [41]. The contour plot of the vertical displacement of the block using the HFS-HEX-8 element

Table 4. Near-incompressible regular block, displacement at the center P of the block.

Element	Displacement
HFS-HEX8	0.02132
HIS [41]	0.01921
3D.EAS-30 [28]	0.01905
QM1/E12 [42]	0.01892

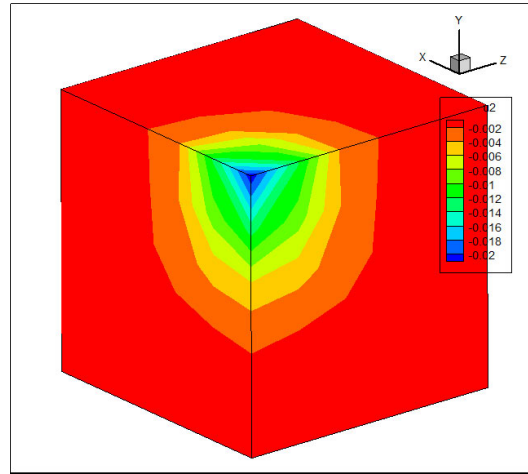


FIG. 23. Contour plot of the vertical displacements of the near-incompressible regular block under central uniform loading.

with $5 \times 5 \times 5$ meshes is shown in Fig. 23. However, it is noted that with the QM1/E12 element, solutions can only be obtained for the two coarsest meshes. For finer mesh resolutions, the QM1/E12 element shows unphysical hourglass instabilities [40].

5. Conclusions

In this work a new HFS-FEM approach has been proposed for analyzing three-dimensional elastic problems. The detailed formulations for three-dimensional HFS-FEM are firstly derived for elastic problems by ignoring body force term and then the method of particular solution and radial basis function approximation are integrated into the HFS-FEM model to solve elastic problems with body forces. The homogeneous solution is obtained by the HFS-FEM and the particular solution by the approach of radial basis function. Several standard tests and numerical examples are presented to demonstrate the capability and accuracy of the method. It is found that the new method with linear 8-node and quadratic 20-node brick elements can successfully pass the patch test. It is also found that HFS-HEX8 element exhibit shear locking phenomenon and cannot pass the Trapezoidal and Parallelogram beam test although it is not very sensitive to the mesh distortion and have a better performance compared to the Pian and Tong's element. In addition, it is demonstrated that the new method usually converges better compared with the traditional FEM and it can be used in problems with nearly incompressible materials without volumetric locking. This new method seems to be promising to deal with the problems

involving complex geometry, stress concentration and multi-materials. It is possible to extend the current method to nonlinear problems by treating nonlinear terms as a generalized body force and developing a convergent iterative algorithm [4, 43].

Acknowledgement

The authors would like to express their sincere thanks to the anonymous reviewers for their helpful comments which significantly improve the quality of the paper.

References

1. J. JIROUSEK, L. GUEX, *The hybrid-Trefftz finite-element model and its application to plate bending*, International Journal for Numerical Methods in Engineering, **23**, 4, 651–693, 1986.
2. Q.H. QIN, *Hybrid Trefftz finite-element approach for plate-bending on an elastic-foundation*, Applied Mathematical Modelling, **18**, 6, 334–339, 1994.
3. J. JIROUSEK, Q.H. QIN, *Application of hybrid-Trefftz element approach to transient heat-conduction analysis*, Computers & Structures, **58**, 1, 195–201, 1995.
4. Q.H. QIN, *Formulation of hybrid Trefftz finite element method for elastoplasticity*, Applied Mathematical Modelling, **29**, 3, 235–252, 2005.
5. H. WANG, Q.H. QIN, D. AROUNSAVAT, *Application of hybrid Trefftz finite element method to non-linear problems of minimal surface*, International Journal for Numerical Methods in Engineering, **69**, 6, 1262–1277, 2007.
6. J.A.T. DE FREITAS, M. TOMA, *Hybrid-Trefftz stress elements for incompressible biphasic media*, International Journal for Numerical Methods in Engineering, **79**, 2, 205–238, 2009.
7. K.Y. SZE, G.H. LIU, *Hybrid-Trefftz six-node triangular finite element models for Helmholtz problem*, Computational Mechanics, **46**, 3, 455–470, 2010.
8. J.A.T. DE FREITAS, I.D. MOLDOVAN, *Hybrid-Trefftz stress element for bounded and unbounded poroelastic media*, International Journal for Numerical Methods in Engineering, **85**, 8, 1280–1305, 2011.
9. Q.H. QIN, *Solving anti-plane problems of piezoelectric materials by the Trefftz finite element approach*, Computational Mechanics, **31**, 6, 461–468, 2003.
10. G.S.A. FAM, Y.F. RASHED, *The Method of Fundamental Solutions applied to 3D structures with body forces using particular solutions*, Computational Mechanics, **36**, 4, 245–254, 2005.
11. C. PATTERSON, M. SHEIKH, *On the use of fundamental solutions in Trefftz method for potential and elasticity problems*, Boundary Element Methods in Engineering, Proceedings of the Fourth International Seminar, Southampton, England, Germany, 21–23 September, 1982, 43–57.

12. R. PILTNER, *The derivation of a thick and thin plate formulation without ad hoc assumptions*, Journal of Elasticity, **29**, 2, 133–173, 1992.
13. J. JIROUSEK, A. WROBLEWSKI, Q.H. QIN, X.Q. HE, *A Family of Quadrilateral Hybrid-Trefftz P-Elements for Thick Plate Analysis*, Computer Methods in Applied Mechanics and Engineering, **127**, 1–4, 315–344, 1995.
14. Q.H. QIN, *The Trefftz Finite and Boundary Element Method*, WIT Press, Southampton 2000.
15. Q.H. QIN, H. WANG, *Matlab and C Programming for Trefftz Finite Element Methods*, CRC Press, New York 2008.
16. H. WANG, Q.H. QIN, *FE approach with green's function as internal trial function for simulating bioheat transfer in the human eye*, Archives of Mechanics, **62**, 6, 493–510, 2010.
17. H. WANG, Q.H. QIN, *Hybrid FEM with fundamental solutions as trial functions for heat conduction simulation*, Acta Mechanica Solida Sinica, **22**, 5, 487–498, 2009.
18. H. WANG, Q.H. QIN, *Fundamental-solution-based finite element model for plane orthotropic elastic bodies*, European Journal of Mechanics, A/Solids, **29**, 5, 801–809, 2010.
19. C. CAO, Q.H. QIN, A. YU, *Hybrid fundamental-solution-based FEM for piezoelectric materials*, Computational Mechanics (to appear).
20. S.W. GAO, Y.S. WANG, Z.M. ZHANG, X.R. MA, *Dual reciprocity boundary element method for flexural waves in thin plate with cutout*, Applied Mathematics and Mechanics-English Edition, **26**, 10, 1564–1573, 2005.
21. M. DHANASEKAR, J.J. HAN, Q.H. QIN, *A hybrid-Trefftz element containing an elliptic hole*, Finite Elements in Analysis and Design, **42**, 14–15, 1314–1323, 2006.
22. S.A. SAUTER, C. SCHWAB, *Boundary Element Methods*, Springer, 2010.
23. C.S. CHEN, C.A. BREBBIA, *The dual reciprocity method for Helmholtz-type operators*, Boundary Elements Xx, **4**, 495–504, 1998.
24. A.H.D. CHENG, C.S. CHEN, M.A. GOLBERG, Y.F. RASHED, *BEM for thermoelasticity and elasticity with body force – a revisit*, Engineering Analysis with Boundary Elements, **25**, 4–5, 377–387, 2001.
25. H. WANG, Q.H. QIN, Y.L. KANG, *A new meshless method for steady-state heat conduction problems in anisotropic and inhomogeneous media*, Archive of Applied Mechanics, **74**, 8, 563–579, 2005.
26. R.H. MACNEAL, R.L. HARDER, *A proposed standard set of problems to test finite element accuracy*, Finite Elements in Analysis and Design, **1**, 1, 3–20, 1985.
27. J. KORELC, P. WRIGGERS, *Improved enhanced strain four-node element with Taylor expansion of the shape functions.*, International Journal for Numerical Methods in Engineering, **40**, 3, 407–421, 1997.
28. U. ANDEFINGER, E. RAMM, *EAS-elements for two-dimensional, three-dimensional, plate and shell structures and their equivalence to HR-elements*, International Journal for Numerical Methods in Engineering, **36**, 6, 1311–1337, 1993.
29. S.L. WEISSMAN, R.L. TAYLOR, *A unified approach to mixed finite element methods: Application to in-plane problems*, Computer Methods in Applied Mechanics and Engineering, **98**, 1, 127–151, 1992.

30. S.L. WEISSMAN, *High-accuracy low-order three-dimensional brick elements*, International Journal for Numerical Methods in Engineering, **39**, 12, 2337–2361, 1996.
31. T.H.H. PIAN, P. TONG, *Relations between incompatible displacement model and hybrid stress model*, International Journal for Numerical Methods in Engineering, **22**, 1, 173–181, 1986.
32. Y.P. CAO, N. HU, J. LU, H. FUKUNAGA, Z.H. YAO, *A 3D brick element based on Hu–Washizu variational principle for mesh distortion*, International Journal for Numerical Methods in Engineering, **53**, 9, 2529–2548, 2002.
33. D.B. RIBEIRO, J.B. PAIVA, *An alternative multi-region BEM technique for three-dimensional elastic problems*, Eng. Anal. Bound. Elem., **33**, 4, 499–507, 2009.
34. J.C. SIMO, M. RIFAI, *A class of mixed assumed strain methods and the method of incompatible modes*, International Journal for Numerical Methods in Engineering, **29**, 6, 1595–1638, 1990.
35. A.H.D. CHENG, C.S. CHEN, M.A. GOLBERG, Y.F. RASHED, *BEM for thermoelasticity and elasticity with body force – a revisit*, Engineering Analysis with Boundary Elements, **25**, 4–5, 377–387, 2001.
36. Z.C. LI, T.T. LU, H.Y. HU, A. CHENG, *Trefftz and collocation methods*, WIT Press, 2008.
37. J.J. GOLECKI, *On stress concentration around circular holes*, International Journal of Fracture, **73**, 1, R15–R17, 1995.
38. G.N. SAVIN, *Stress Concentration Around Holes*, Pergamon Press, New York 1961.
39. E.S. FOLIAS, J.J. WANG, *On the three-dimensional stress field around a circular hole in a plate of arbitrary thickness*, Computational Mechanics, **6**, 5, 379–391, 1990.
40. D.S. MUELLER-HOEPPE, S. LOEHNERT, P. WRIGGERS, *A finite deformation brick element with inhomogeneous mode enhancement*, International Journal for Numerical Methods in Engineering, **78**, 8, 1164–1187, 2009.
41. P.M.A. AREIAS, J.M.A. CÉSAR DE SÁ, C.A.C. ANTÓNIO, A.A. FERNANDES, *Analysis of 3D problems using a new enhanced strain hexahedral element*, International Journal for Numerical Methods in Engineering, **58**, 9, 1637–1682, 2003.
42. J. KORELC, P. WRIGGERS, *An efficient 3D enhanced strain element with Taylor expansion of the shape functions*, Computational Mechanics, **19**, 2, 30–40, 1996.
43. Q.H. QIN, *Postbuckling analysis of thin plates by a hybrid Trefftz finite element method*, Computer Methods in Applied Mechanics and Engineering, **128**, 1–2, 123–136, 1995.

Received July 4, 2011; revised version February 8, 2012.
